Acta Astronautica 238 (2026) 320–334

Contents lists available at ScienceDirect

Acta Astronautica

journal homepage: www.elsevier.com/locate/actaastro

Impact of thermal protections insulation layer on solid rocket motor residual thrust

F. Ponti [a,*], S. Mini [a], V. Ravaglioli [a], A. Annovazzi [b], M. Fiorillo [c], E. Gizzi [c]

[a] University of Bologna, Forlì, FC, Department DIN, Via Fontanelle 40, 47121, Italy
[b] Colleferro, Rome, 00034, Italy
[c] Design Department, Avio Space Propulsion, Colleferro, Rome, 00034, Italy

ABSTRACT

The aim of the paper is to reproduce thermal protection ablation in solid rocket motors focusing on how it affects rocket performance. A physical model able to predict thermal protection ablation behavior coupled with an internal ballistic simulator is outlined. The main outcome of the above-mentioned model is the estimation of the residual thrust occurring after burn-out at high altitudes. The evaluation of the residual thrust is especially important for solid rocket motors used as upper stages and after burn-out operations take place in vacuum. During these phases, residual thrust is generated by the expansion of pyrolysis gases produced by the ablation of thermal protection materials. The nozzle radiative power was identified as the main source causing thermal protection material to ablate. An investigation of a commercial motor performance is conducted and discussed. A detailed explanation of the numerical methods used is provided.

1. Introduction

The aim of the present work is to evaluate the impact of case thermal protections on *SRM* performance and, in particular, on the tail-off thrust time profile because of nozzle radiation. As a matter of fact, for upper stages, the usually negligible mass flow rate of hot gases, generated by thermal protection ablation, expanding into vacuum, leads to thrust contribution capable of accelerating again the system especially during and after tail-off. Knowing tail-off thrust of solid rocket motors (*SRMs*) used as the upper stage of launch vehicles is essential for proper sequencing of stage separation, and to design and manage interstage wait times and separation systems total impulse accurately. As reported also by experimental observations [1], upper stages *SRM* tail-off can last tens of seconds after the theoretical burn-out time, thus causing a significative total impulse. The total impulse generated by such tail-off thrust has to be estimated and accounted for when designing the separation system. In past literature [1,2], it is shown that pyrolysis gases responsible for the residual thrust are mainly produced by alumina deposited within the motor at the end of the burning phase, namely slag [3,4]. *SRMs* tend to accumulate significant amounts of slag [5,6] in the region around the submerged nozzle [7,8], leading to both degradation of motor performance [9] and control problems in terms of vehicle instability [10]. Furthermore, molten slag acts as a radiative heat source causing thermal protections to ablate even when propellant grain combustion is over [11,12]. In order to estimate this phenomenon, usually semi-empirical models are used based on experimental observations [13,14]. Other works have been developed with the scope of estimating the amount of gases being developed by the pyrolysis process when a heat source is contributing to the heating of the thermal protection [15,16]; this is usually done through models capable of describing the phenomena occurring on the surface of an ablative material [17,18], in some cases with a very accurate description of the multi-dimensional phenomenon [19,20]. This study further develops these concepts, showing that in motors where slag is not present another heat source can give rise to residual thrust: indeed, the region of the nozzle within the combustion chamber (Fig. 1), warmed up by combustion chamber hot gases during propellant grain burning, releases radiative power after burn-out, behaving in the same way as alumina slag effect outlined before.

The above-mentioned interaction between thermal protections and nozzle during tail-off phase is studied following a two-step approach. First, a mathematical-physical model of thermal protections is established to generate maps including two output parameters: pyrolysis gas mass flow rate generated by the virgin material and combustion chamber heat power absorbed by thermal protection due to the endothermic chemical reaction of ablation. Subsequently, those maps are integrated in *ROBOOST* (Rocket BOOst Simulation Tool), an internal ballistic simulator able to evaluate *SRMs* combustion surface regression, fluid dynamics, grain anisotropies [21] and tail-off effects [22]. Integrating

* Corresponding author.
E-mail addresses: fabrizio.ponti@unibo.it (F. Ponti), ste.mini91@gmail.com (S. Mini), vittorio.ravaglioli2@unibo.it (V. Ravaglioli), annadrian6@outlook.it (A. Annovazzi), marco.fiorillo@avio.com (M. Fiorillo), emanuela.gizzi@avio.com (E. Gizzi).

https://doi.org/10.1016/j.actaastro.2025.09.092
Received 16 December 2024; Received in revised form 9 September 2025; Accepted 28 September 2025
Available online 6 October 2025

I. nomenclature

Latin

A	= cross-section thermal protection material area, m^2
A_{TP}	= thermal protection material area, m^2
B	= Arrhenius constant, $1/s$
c_P	= specific heat, $J/kg{\cdot}K$
E_a	= Arrhenius activation energy per unit mole, $J/\ mol$
H	= enthalpy per unit mass, J/kg
$\overline{H}$	= weighted average enthalpy per unit mass, $J/\ kg$
K_1	= first char erosion constant, $m^2{\cdot}K/W$
K_2	= second char erosion constant, -
h_c	= heat transfer convective coefficient, $W/m^2{\cdot}K$
k	= thermal conductivity, $W/m{\cdot}K$
L	= thermal protections thickness, m
M	= mass flow rate per unit surface, $kg/s{\cdot}m^2$
$\dot{m}$	= mass flow rate, kg/s
$\dot{m}_{gas_{core}}$	= combustion gas mass flow rate linked to combustion chamber core, kg/s
$\dot{m}_{gas_{tr}}$	= mass flow rate linked to transpiring gas, $kg/\ s$
$\dot{Q}_{abs}$	= thermal power absorbed by ablative material from combustion chamber per unit surface, W/m^2
$\dot{Q}_{cond}$	= thermal conduction power per unit surface, $W/\ m^2$
$\dot{Q}_{conv}$	= thermal convective power per unit surface, $W/\ m^2$
$\dot{Q}_{in}$	= chemical power per unit surface from in-depth material, W/m^2
$\dot{Q}_{noz}$	= nozzle radiative power per unit surface, $W/\ m^2$
$\dot{Q}_{out}$	= chemical power per unit surface exiting from the material due to blowing effect, W/m^2
$\dot{Q}_{rad_{in}}$	= radiative power per unit surface entering the material, W/m^2
$\dot{Q}_{rad_{out}}$	= radiative power per unit surface exiting the material, $W/\ m^2$
R	= universal gas constant, $J/mol{\cdot}K$
r_b	= propellant burning rate, m/s
$\dot{s}$	= char recession rate, m/s
t	= time, s
t_0	= reference time instant, s
T	= temperature, K
T_I	= initial thermal protection temperature, K
T_0	= formation temperature, K
V_F	= view factor between nozzle and rocket case
x	= spatial coordinate, m

Greek

α	= weighted average between virgin material and char specific heats, $J/kg{\cdot}K$
α_s	= ablative material absorptivity, -
β	= weighted average between virgin material and char specific heats difference, $J/kg{\cdot}K$
ε	= emissivity, -
θ	= time in fixed coordinate reference frame, s
η	= weighted average between virgin material and char thermal conductivities, $W/m{\cdot}K$
ξ	= weighted average between virgin material and char conductivities difference, $W/m{\cdot}K$
ρ	= density, kg/m^3
σ	= Stefan-Boltzmann constant, $W/m^2{\cdot}K^4$
φ	= blowing parameter, -
X	= virgin material mass fraction, -
ψ	= Arrhenius exponent, -
τ	= gas shielding factor linked to optical length
Ω_v	= virgin material volume fraction

Subscripts

c	= char material
g	= pyrolysis gas
gas	= combustion chamber hot gases
p	= propellant
v	= virgin material

Superscript

$'$	= integration variable
o	= formation enthalpy

Acronyms

CEA	= Chemical Equilibrium and Applications
CMA	= Charring Material thermal response and Ablation program
FIAT	= Fully Implicit Ablation and Thermal analysis program
HTPB	= Hydroxyl-Terminated PolyButadiene
NASA	= National Aeronautics and Space Administration
PATO	= Porous material Analysis TOolbox
ROBOOST	= Rocket BOOst Simulation Tool
SRM	= Solid Rocket Motor
Z9	= ZEFIRO 9 (ZEro FIrst stage ROcket 9)

the thermal protection ablation model is possible since *ROBOOST* can evaluate at each time instant the extension and 3D location of the thermal protection surface exposed to ablation. The outcome is the residual thrust evolution in time linked to tail-off. The previously mentioned procedure is applied to ZEFIRO 9 (*Z9*), namely the third stage of Vega launcher. Vega is a single body launcher designed to launch small payloads (up to 1500 *kg*) to low Earth orbits, consisting of three solid rocket stages and one liquid engine upper stage. More precisely, *Z9* (Fig. 1) is the last and smallest of the three solid rocket stages.

In contrast to previous studies that attribute residual thrust primarily to slag accumulation, this work introduces then a novel perspective by identifying nozzle radiative heating as a significant contributor to thermal protection ablation and, consequently, to residual thrust. The originality of the proposed model lies in its tight coupling between a physical ablation model and a detailed internal ballistic simulation capable of accounting for nozzle radiation effects during the tail-off phase. Unlike empirical or 1D isolated thermal models, the developed approach enables a dynamic, time-resolved prediction of residual thrust by integrating multi-parametric thermal protection maps within a full SRM simulation environment. This integration allows for accurate estimation of thrust profiles even after burn-out, which is critical for upper-stage separation logic and mission planning. Additionally, the model is validated across multiple SRM configurations, demonstrating both its predictive power and adaptability to different thermal protection materials and nozzle geometries.

2. Thermal protection ablation mathematical model

2.1. Comparison with previous works

Polymeric composites have been used as ablative thermal protection systems for a variety of military and aerospace applications. More specifically, the term *ablative* includes all the physicochemical processes (sublimation, chemical reactions, and erosion) linked to surface material removal effects [23]. The incoming thermal loads are restrained since the material changes state of matter (from solid to liquid or gas)

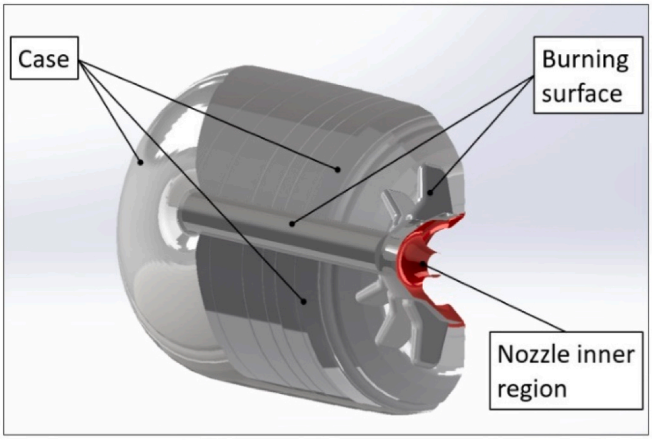

Fig. 1. ZEFIRO 9 layout.

absorbing most part of the thermal energy close to the wall and maintaining the underlying structure within acceptable temperature limits [24]. Therefore, thermal protection materials are marked out by low thermal conductivity, high heat capacity and large heat of degradation, thus working as an effective barrier against an extreme temperature environment [25]. Those materials are commonly divided in two categories [26]: *charring* ablators and *non-charring* ablators. C*harring* materials are essentially fibrous materials injected with resin that binds the material adding higher mechanical strength [27,28]. Chemical decomposition of the virgin material leads to the generation of gaseous products (mainly hydrocarbons) and carbonaceous products (char). Fig. 2 shows the different layers describing the ablation phenomenon of charring materials in the *SRM* combustion chamber environment. More in detail, char chemical reactions between the material at the surface and the boundary layer species (linked to combustion chamber hot gases) could lead to a recession of the abovementioned material surface. Moreover, those reactions occur both in the decomposition zone and between the char zone and the hot gases one. Instead, *non-charring* materials do not show any pyrolysis phenomenon and chemical reactions are exclusively localized on the surface of the material [29].

Furthermore, ablative materials can be divided according to the operating performance of the surface layer in contact with the high temperature environment: depending on the melting of the abovementioned layer there are *melting* or *subliming* ablators and *non-melting* ablators [30]. *Subliming* ablators behave as a heat sink until the surface reaches the melting temperature, then their effect is to remove heat from

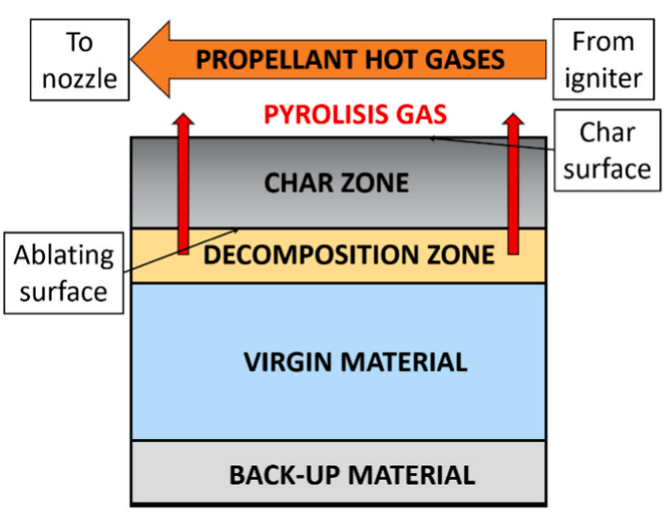

Fig. 2. thermal protection *charring* material.

the insulation material. *Non-melting* materials act as a heat sink up to partial sublimation following which they start producing pyrolysis gas: a typical example are *charring ablators* (Fig. 2).

In order to evaluate the impact of the thermal protections case insulations on *SRM* performance, a reliable numerical simulator is needed to evaluate the tight coupling between combustion chamber thermo-fluid dynamics and thermal protections surface recession rate under general heating conditions.

The program *CMA* (Charring Material thermal response and Ablation program [31]) is a finite-difference computational procedure treating the one-dimensional transient transport of thermal energy in 1D isotropic material which can ablate from a front surface and can decompose in-depth. It underlies a wide range of problems of technical interest simulating the material before and after ablation as virgin plastic becoming solid char and gaseous product. However, *CMA* solutions are very sensitive to user time step choice since time discretization is performed with an explicit method used to obtain recession rate as well [32]. For this reason, *FIAT* (Fully Implicit Ablation and Thermal analysis program) [33,34] has been introduced to overcome the abovementioned disadvantage. In the same way as *CMA*, this code is based on a finite-difference approach performed on a moving grid system. However, the availability of these codes to the research community is often restricted. Moreover, in Refs. [27,28], it is pointed out a 1D heat and mass transfer model based on finite element technique with first and second implicit time integrators. Finite volume discretization is employed to solve a thermal equilibrium model for porous reactive materials subjected to high temperatures.

Recently new multi-dimensional methodologies have been proposed to examine the consumption of the re-entry vehicle shields: these models consist of a coupling between high fidelity thermal protection shield code and a hypersonic fluid dynamic solver. That model has been implemented in *PATO* (Porous Material Analysis Toolbox) [35–37]. In addition, both finite element and finite volume strategies are employed to perform a tight coupling between hypersonic aerodynamic heating and structural heat transfer. A 3D fluid-structural numerical method is established due to the strong impact of re-entry aerodynamics. Finally, commercial codes are also considered in ablation numerical predictions. The commercial software used in Refs. [38,39] does not consider the modeling and simulation of material decomposition heat losses and surface material removal. Simulations are numerically performed using finite element methods.

The present study deals with *charring ablators* used to insulate *SRMs* combustion chamber case, preventing it from being exposed to high temperatures [40]. A 1D model is developed to predict both material recession and ablation products. In fact, *SRMs* case geometry is often equivalent to a cylinder with a circular cross-section surface, and thus a multi-dimensional model does not offer any meaningful advantage in terms of simulation results. As outlined in the previous paragraph, 2D or 3D models are mostly considered for re-entry vehicle shields which have more complex geometries. In that case, 2D or 3D effects are no longer negligible and take an important role in performance evaluation. Moreover, because of 1D ablation model, the finite difference method proves to be a more suitable numerical technique to 1D models with simple geometries compared to the finite element method [41]. On the other hand, a finite difference mesh would need a higher number of nodes close to the boundary of complex geometries, resulting in a substantial increase in computational time and effort.

2.2. Model description

Analysis of a complete transient *charring* material ablation problem is strictly coupled with the need for including the transient heat conduction phenomenon within the computation itself. Therefore, thermal protection ablation and material consumption have been modelled using the following assumptions [42]: heat thermal conduction is one-dimensional, perpendicular to thermal protection surface (Fig. 3);

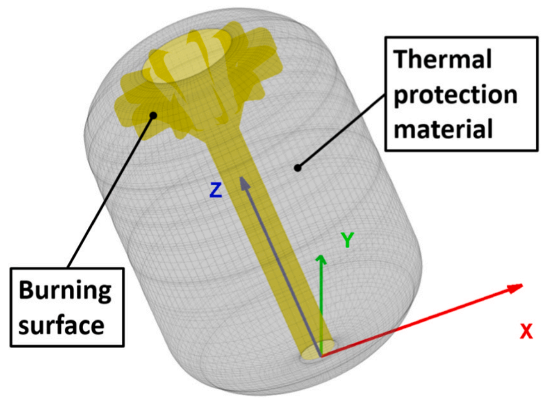

Fig. 3. Ablation model global reference frame.

any pyrolysis gases formed are in thermal equilibrium with the char; no chemical reaction between pyrolysis gas and char is taking place; any pyrolysis gas formed is assumed to go immediately out through the char meaning zero residence time in the char itself; chemical decomposition rate is evaluated using an Arrhenius type of expression.

The assumptions that pyrolysis gases do not react chemically with the char layer and have zero residence time within it are commonly adopted in simplified 1D ablation models, especially when the primary goal is to capture the dominant energy transfer mechanisms and provide a computationally efficient framework for integration with internal ballistic simulations. While it is true that in a high-temperature porous medium like char, pyrolysis gases can undergo secondary reactions or experience flow resistance, accounting for these phenomena would require a more detailed porous flow model, such as those found in multi-dimensional CFD-porous media coupling frameworks, significantly increasing model complexity and computational cost. In the present context, which focuses on tail-off thrust prediction these simplifications are considered acceptable. Nonetheless, it is acknowledged that this approach might slightly underestimate gas-solid interaction effects within the char layer.

It is also worth noting that while the generation of pyrolysis gases plays a central role in the tail-off thrust investigated in this work, the chemical details of the pyrolysis reactions themselves are not the primary focus of the study. Instead of explicitly modeling the complex reaction pathways, the properties of the pyrolysis gases (composition, enthalpy, specific heat, etc.) have been obtained using the NASA Chemical Equilibrium and Applications (*CEA*) program, which assumes equilibrium chemistry for a predefined material composition. This approach ensures consistency and reliability in defining thermodynamic parameters without delving into detailed chemical kinetics, which would significantly increase model complexity. Since the main novelty of this work lies in the integration of ablative material response with ballistic performance predictions (particularly residual thrust estimation via nozzle radiative feedback), a more detailed chemical reaction network was considered beyond the scope of this paper. Future developments may incorporate a more detailed reaction mechanism where needed, as well as a more refined treatment of porous flow dynamics to assess their influence on gas generation and surface energy balance.

It is possible to treat the decomposition in other ways, such as considering density as a function of temperature, or in an easier way, converting virgin material to complete char at one specified temperature. However, an Arrhenius relation is often considered since it is easy to be computed numerically and guarantees reliable predictions despite being simple [43]. Equations moving coordinate system is located on the receding surface (char surface, Fig. 4); partial differential equations [31] are considered in a local reference frame, close to the case, along x direction (Fig. 4), varying with char material position at each time.

They consist of a mass balance (Eq. (1)), an Arrhenius expression (Eq.

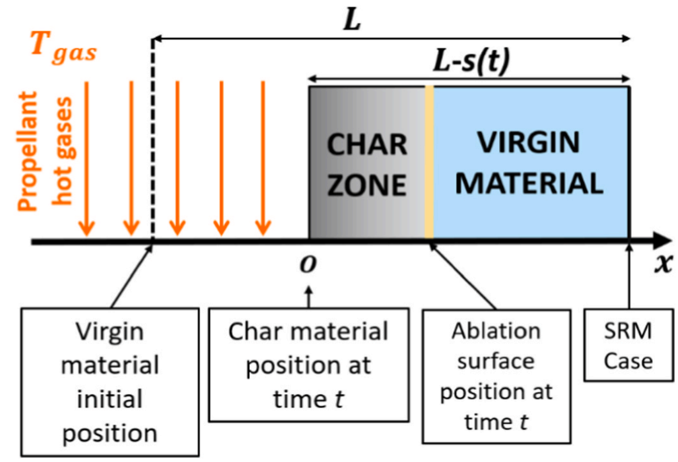

Fig. 4. Ablation model local reference frame.

(2)) linked to material density variation, and an energy balance (Eq. (3)), all of them dependent on time t and space x.

$$\frac{\partial \rho}{\partial t} = \dot{s}\frac{\partial \rho}{\partial x} + \frac{\partial M_g}{\partial x} \tag{1}$$

$$\frac{\partial \rho}{\partial t} = \dot{s}\frac{\partial \rho}{\partial x} - B\rho_v e^{-\frac{E_a}{RT}}\left(\frac{\rho - \rho_c}{\rho_v}\right)^{\psi} \tag{2}$$

$$\begin{aligned}\frac{\partial T}{\partial t} = \frac{1}{\alpha\rho - \beta}\Bigg\{ &\left(H_g - \overline{H}\right)\frac{\partial M_g}{\partial x} + \Bigg[\dot{s}(\alpha\rho - \beta) + M_g c_{p_g} + \frac{\xi}{\rho^2}\frac{\partial \rho}{\partial x} \\ &+ \left(\frac{\rho_v}{\rho_v - \rho_c}\left(1 - \frac{\rho_c}{\rho}\right)\left(\frac{dk_v}{dT} - \frac{dk_c}{dT}\right) + \frac{dk_c}{dT}\right)\frac{\partial T}{\partial x}\Bigg]\frac{\partial T}{\partial x} + \left(\eta - \frac{\xi}{\rho}\right)\frac{\partial^2 T}{\partial x^2}\Bigg\}\end{aligned} \tag{3}$$

where:

$$\alpha = \frac{c_{p_v}\rho_v - c_{p_c}\rho_c}{\rho_v - \rho_c} \tag{4}$$

$$\beta = \left(c_{p_v} - c_{p_c}\right)\frac{\rho_v \rho_c}{\rho_v - \rho_c} \tag{5}$$

$$\xi = (k_v - k_c)\frac{\rho_v \rho_c}{\rho_v - \rho_c} \tag{6}$$

$$\eta = \frac{k_v \rho_v - k_c \rho_c}{\rho_v - \rho_c} \tag{7}$$

$$\overline{H} = \frac{\rho_v H_v - \rho_c H_c}{\rho_v - \rho_c} \tag{8}$$

$$H_g = H_g^0 + \int_{T_0}^{T} c_{p_g}(T')dT' \tag{9}$$

$$H_v = H_v^0 + \int_{T_0}^{T} c_{p_v}(T')dT' \tag{10}$$

$$H_c = H_c^0 + \int_{T_0}^{T} c_{p_c}(T')dT' \tag{11}$$

Equations (1)–(3) represent the mathematical-physical ablation model regarding the in-depth solution, namely the solution within the ablative material without the boundaries. Solution vector consists of the following functions varying with time t and space x: material density ρ, material temperature T and pyrolysis gas mass flow rate per unit surface M_g. On the other hand, Equations (4)–(11) are simply coefficients definitions as functions of material thermal properties (specific heat at constant pressure, thermal conductivity, formation enthalpy and density). It is important to notice that these properties (except density) are generically temperature dependent: this clarifies why in Eq. (3) temperature derivatives of thermal conductivity are required. It is fundamental to highlight that Eq. (1) represents the conservation of the total mass, i.e., char material, virgin material, and pyrolysis gases. $\frac{\partial \rho}{\partial t} - \dot{s}\frac{\partial \rho}{\partial x}$ represents solid material local density time variation, expressed according to the moving reference frame (Fig. 4). $\frac{\partial M_g}{\partial x}$ determines the variation regarding pyrolysis gases mass flow rate per unit surface along the spatial coordinate x. Indeed, during the material pyrolysis, the density time variation linked to the material solid part (from virgin to char material) is equal to the spatial variation of pyrolysis gases mass flow rate per unit surface ($\frac{\partial M_g}{\partial x}$) meaning that there is a portion of solid material which sublimates into gaseous products, i.e., pyrolysis gases. On the other hand, Eq. (2) represents mass conservation of solid material part only. In fact, Eq. (2) defines how the virgin material consumption is modelled. It is not meant to substitute Eq. (1), since Eq. (2) simply regards the pyrolysis reaction kinetics, modelled as a one-step reaction. More details on the development of Eq. (3) and on the meaning of the corresponding coefficients is presented in Appendix A.

The initial conditions needed to solve the above-mentioned model are outlined in Eq.s (12)–(14). Equation (12) states that no ablation takes place at initial time, then material density coincides with virgin material density as well. For the same reason, there is no pyrolysis gas mass flow rate per unit surface produced (Eq. (13)) and temperature spatial distribution is equal to initial temperature profile (Eq. (14)).

$$\rho(t=0,x)=\rho_v \tag{12}$$

$$M_g(t=0,x)=0 \tag{13}$$

$$T(t=0,x)=T_I \tag{14}$$

Boundary conditions are (Eq.s (15)–(17)):

$$M_g(t,x=L-s)=0 \tag{15}$$

$$\dot{Q}_{conv}+\dot{Q}_{rad_{in}}-\dot{Q}_{rad_{out}}-\dot{Q}_{out}+\dot{Q}_{in}-\dot{Q}_{cond}=0 \tag{16}$$

where:

$$s=\left(1-K_1 h_c e^{-K_2\frac{\dot{m}_{gas_{tr}}}{\dot{m}_{gas_{core}}}}\right)\int_o^t \dot{s}(t')dt' \tag{17}$$

Eq. (15) is valid at *SRM* case, meaning that no pyrolysis gas flow rate crosses the wall. Since a moving reference frame is used to solve the model tied to char recession surface, wall relative coordinate is $x = L - s$ depending on char recession rate (Eq. (17)). It is assumed that, in a similar way to propellant erosion, char mechanical erosion is caused by the action of combustion gas flow towards the char-free surface. It is acknowledged that the physical and chemical properties of char differ significantly from those of the virgin propellant, and thus the erosion mechanisms may also differ. In this work, this approach is adopted as a first-order approximation to account for the observed shear-induced char removal due to high-velocity gas flow, which acts tangentially on the char surface in a manner somewhat similar to erosive effects on propellant. While this model provides a practical and computationally efficient way to include mechanical erosion in the simulation, it is acknowledged that this may not capture all relevant microstructural or thermomechanical phenomena specific to char.

As a matter of fact, combustion gas flow produces physical drag towards the char layer exposed to the combustion chamber causing the occurrence of shear stresses that reduce char thickness. Therefore, according to erosive burning model [42], it has been considered the term $h_c e^{-K_2\frac{\dot{m}_{gas_{tr}}}{\dot{m}_{gas_{core}}}}$ to model the char erosion, where the two constants K_1 and K_2 have been conveniently chosen and are respectively equal to $3{\cdot}10^{-6}$ $\frac{m^2K}{W}$ and 0.5. Char recession surface boundary condition (Eq. (16)) requires special treatment since it includes many different phenomena occurring at the material surface [43] (Fig. 5).

The various contributions are explicitly reported in the following equations (Eq. (18) to Eq. (23)).

$$\dot{Q}_{conv}=h_c\frac{\varphi}{e^{\varphi}-1}\left(T_{gas}-T(t,x=0)\right) \tag{18}$$

$$\dot{Q}_{rad_{in}}=\alpha_s\sigma\varepsilon_{gas}T_{gas}^4+\tau V_F\dot{Q}_{noz} \tag{19}$$

$$\dot{Q}_{rad_{out}}=\sigma\varepsilon_{TP}T^4(t,x=0) \tag{20}$$

$$\dot{Q}_{out}=-\left(M_c+M_g(t,x=0)\right)\left(H_{gas}^0+\int_{T_0}^{T(t,x=0)}c_{p_{gas}}(T')dT'\right) \tag{21}$$

$$\dot{Q}_{in}=\dot{Q}_{in_1}+\dot{Q}_{in_2}=M_cH_c(T=T(t,x=0))+M_g(t,x=0)H_g(T=T(t,x=0)) \tag{22}$$

$$\dot{Q}_{cond}=-k(t,x=0)\left.\frac{\partial T}{\partial x}\right|_{t,x=0} \tag{23}$$

where:

$$\varphi=\frac{2\lambda\left(M_c+M_g(t,x=0)\right)c_{p_{gas}}}{h_c} \tag{24}$$

$$k(t,x)=\mathrm{X}(t,x)k_v+(1-\mathrm{X}(t,x))k_c \tag{25}$$

$$\mathrm{X}(t,x)=\frac{\rho_v}{\rho_v-\rho_c}\left(1-\frac{\rho_c}{\rho}\right) \tag{26}$$

Equation (18) regards the convection heat transfer between the combustion chamber hot gases boundary layer and the char surface. The value $\varphi/_{e^{\varphi}-1}$ is linked to the blowing rate correction accounting for boundary layer blowing effects [31]. Parameter φ depends on λ non-dimensional coefficient related to combustion chamber flow regime (Eq. (24)). More in detail, λ is an experimental blowing correction fitting parameter aimed at including specific effects such as molecular weight effects. A value of $\lambda = 0.4$ appears to be appropriate to correlate constant-properties turbulent flow data [31].

It is important to highlight that the coefficient α_s (Eq. (19)) represents ablative material absorptivity in a two-phase gas mixture where

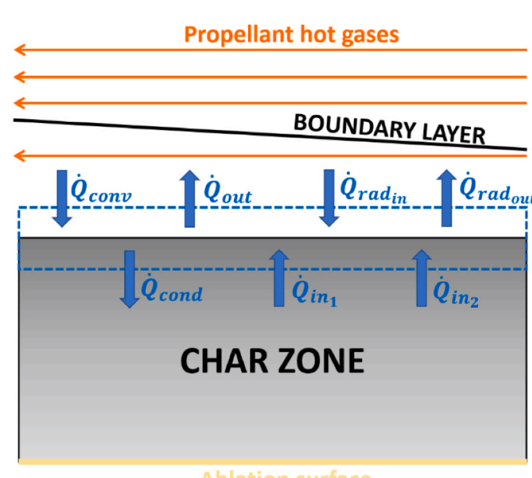

Fig. 5. Energy balance at the char recession surface.

one phase is gaseous, and the other consists of monodispersed alumina particles [44]. The algebraic sum of $\dot{Q}_{in} - \dot{Q}_{out}$ represents the net of several fluxes of chemical energies at the surface. More in detail, $\dot{Q}_{in}$ (Eq. (22)) is associated to the energy fluxes arriving at the char surface from within the solid material and $\dot{Q}_{out}$ (Eq. (21)) is related to the power leaving the char surface in the gross motion (blowing) of the gas adjacent to the surface (Fig. 5). Finally, Equation (23) is linked to the amount of power crossing the ablative material with a conduction heat transfer propagation. It is fundamental to notice that thermal conductivity k of the overall material is expressed as a weighted average (Eq. (25)) of thermal conductivity of virgin material k_v and of char material k_c, [43]. The average weight X is the mass fraction of virgin material (Eq. (26)).

Radiative heat transfers directed inward and outward with respect to the blue control surface (Fig. 5), are respectively modelled with Eq. (19) and Eq. (20). Equation (19) includes nozzle power $\dot{Q}_{noz}$ coming from the nozzle temperature model of *ROBOOST* [45]. The nozzle temperature, which governs the radiative power emitted toward the thermal protection surfaces, is estimated using a sub-model within the *ROBOOST* simulation environment. This model balances the energy absorbed by the nozzle structure during combustion (via convective and radiative heat fluxes from the grain gases) with the energy it emits through surface radiation. $\dot{Q}_{noz}$ is estimated considering the heat exchange among the inner part of the nozzle structure, its surface and the convective/radiative heat coming from the grain combustion. In the first phase, after *SRM* ignition, the heat flux entering the nozzle material is larger than the heat flux radiated by its surface and nozzle temperature increases. When combustion heat flux its operative temperature in the order of 3000 K, it starts radiating power to the nozzle surface. Due to the shielding effect of grain combustion gases within the combustion chamber, the insulating material is not highly affected by nozzle radiative flux during the quasi-steady state phase operation of the motor. A combustion gas shielding factor τ depending on combustion chamber pressure is used to estimate the change in time of absorbing gas properties. τ varies between 0 and 1 according to the entity of gases optical length [46]. When combustion chamber pressure is high, optical length is expected to be small also due to the absorption and re-emission characteristics of CO_2 and H_2O in the infrared spectrum, and thus τ tends to 0. On the contrary, low combustion chamber pressure implies a large optical length meaning that τ is near 1. The dependence between the shielding parameter and the pressure is linear [46]. At the end of grain combustion, i.e., close to burn-out time, pressure is lower, and the shielding effect is reduced; radiative power coming from the nozzle reaches the thermal protection surface with different intensities, depending on the local view factor V_F (blue curve in Fig. 6). In this work, a black-body assumption (i.e., emissivity $\varepsilon = 1$) has been adopted to model the nozzle's radiative emission, primarily as a conservative estimate of the thermal load on the thermal protection surface. It is acknowledged that in reality, the nozzle surface is composed of composite materials with heterogeneous structure and non-negligible roughness, which typically results in an emissivity lower than unity. However, the black-body assumption ensures an upper-bound estimation of the radiative power, which is appropriate for the scope of this work.

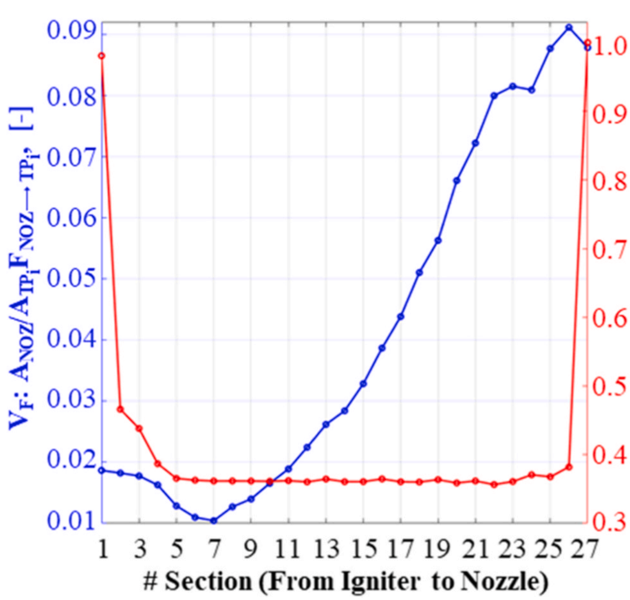

Fig. 6. View factor distribution along motor axis z.

To compute such trend, *Z9* thermal protection case is split into 27 axisymmetric annular sections perpendicular to the motor axis z (Fig. 3). For each annular section, both thermal protection area (red curve in Fig. 6) and view factor are determined through a commercial software [47]. More precisely, Fig. 6 shows the non-dimensional thermal protection area A_{TP_i} (obtained by dividing the thermal protection surface linked to each annular section with respect to the maximum area among the *SRM* sections).

In order to obtain char recession rate $\dot{s}$ (defined in Eq. (27)), mass conservation equation (Eq. (1)) must be integrated at the gas-solid interface of a generic planar pyrolyzing ablative material [48].

$$\dot{s} = \frac{M_c}{\rho_c} \tag{27}$$

Considering the steady-state solution only, the integrated mass conservation equation in a moving coordinate system is:

$$M_c + M_g(t, x = 0) = \rho_v \dot{s} \tag{28}$$

Mass conservation steady-state assumption implies that the thickness of the charred material does not vary with time anymore. Coupling Eq. (27) with Eq. (28), the final formulation of char recession rate is:

$$\dot{s} = \frac{M_g(t, x = 0)}{\rho_v - \rho_c} \tag{29}$$

Equation (29) allows the quantification of the char mass flow rate per unit surface as well, once pyrolysis gas mass flow rate per unit surface is known.

3. Algorithm overview

3.1. Thermal protections simulation: maps generation

Solution of the in-depth response varying with time and space (Eqs. (1)–(3)) is obtained by applying the finite difference technique. A high order approximation of the space derivative is required for an accurate solution since, for most common materials, the density profile, representing degradation from virgin material to char, has a steep spatial gradient. Furthermore, different spatial numerical stencils are used depending on the equation considered. A 4^{th}-order forward difference formula has been used for Eq. (1) and Eq. (2) because the information propagates from left (at $x = 0$) to right (at $x = L - s$) with velocity $\dot{s}$. A 4^{th}-order central scheme has been used for Eq. (3), where the diffusion mechanism dominates with the same order of magnitude in all directions. Time discretization needs a different treatment. Because of the significant non-linearity and strict coupling of the system, time derivative should be approximated with implicit methods, thereby increasing the accuracy of the approximation. Backward difference formula of the 2^{nd} order has been chosen, and for this reason, according to its stencil, the estimation of function derivative at a certain time instant is computed using information from two already computed time points. Boundary conditions discretization are the following: Eq. (16) is numerically computed using 4^{th}-order forward spatial scheme, Eq. (15) is discretized with a 4^{th}-order backward spatial scheme.

By solving Eq.s (1)–(29) and setting input values T_{gas}, h_c and $\dot{Q}_{noz}$, it is possible to obtain the time evolution of M_g, T, ρ and the value of the absorbed power $\dot{Q}_{abs}$. Simulation initial conditions are ambient temperature and pressure. Since such values greatly differ from the actual working conditions of the thermal protection surface, the most interesting part of each simulation is the steady-state condition reached at the end of the initial transient, after approximately 15s. With the aim of capturing the tail-off behavior of *Z9*, h_c varies from a peak of 1500 $W/_{m2K}$, during thrust quasi-steady state phase to nearly 0 $W/_{m^2K}$ after the end of grain combustion; the gas temperature (T_{gas}) ranges from 3500 K to the initial environment temperature T_I; $\dot{Q}_{noz}$ varies between 0 and $3.7{\cdot}10^6$ $W/_{m2}$. The results obtained from the different simulations are collected into maps. Maps input parameters are combustion chamber hot gases temperature, T_{gas}, heat transfer convective coefficient, h_c (linked to combustion chamber fluid dynamics), and nozzle radiative power per unit surface; output parameters are pyrolysis gas mass flow rate per unit surface, $M_g(t, x = 0)$, char recession rate, pyrolysis gas temperature at the exit, $T(t,x = 0)$, and power per unit surface absorbed by ablation chemical process. The evaluation of T_{gas} is performed starting from *HTPB*-based propellant thermochemical properties. Such properties are used to obtain grain combustion reference temperature through *NASA CEA* (Chemical Equilibrium and Applications) program. Then, combustion chamber hot gases temperature (T_{gas}) is estimated through the internal ballistics model linked to *ROBOOST* program. At each simulation time instant, temperature distribution along the motor axis is computed considering the energy balance within the combustion chamber. The heat transfer convective coefficient (h_c) linked to the combustion chamber high temperature flow is evaluated through the Dittus-Boelter formula integrated in *ROBOOST*. The last input value of the maps is the nozzle radiative power per unit surface ($\dot{Q}_{noz}$). It is important to emphasize that the above-mentioned absorbed power $\dot{Q}_{abs}$ is the net power absorbed by thermal protections from combustion chamber hot gases only, without taking into account nozzle radiative power. The multidimensional map collecting the simulation results is implemented as a set of 3 tridimensional maps, each of them associated to a different value of $\dot{Q}_{noz}$ and repeating for that value of $\dot{Q}_{noz}$ the effects due to T_{gas} and h_c. To verify that the steady-state values collected into the maps can describe the thermal protection behavior even under input changing conditions (h_c, T_{gas}, $\dot{Q}_{noz}$), dedicated simulations have been performed applying step variations of each of the inputs. Fig. 7 shows how pyrolysis gas mass flow rate varies with time when nozzle radiating power per unit surface corresponding to tail-off phase is applied to the thermal protection at steady-state initial conditions. The black line represents the steady state value obtained with the trend of nozzle radiating power at tail-off.

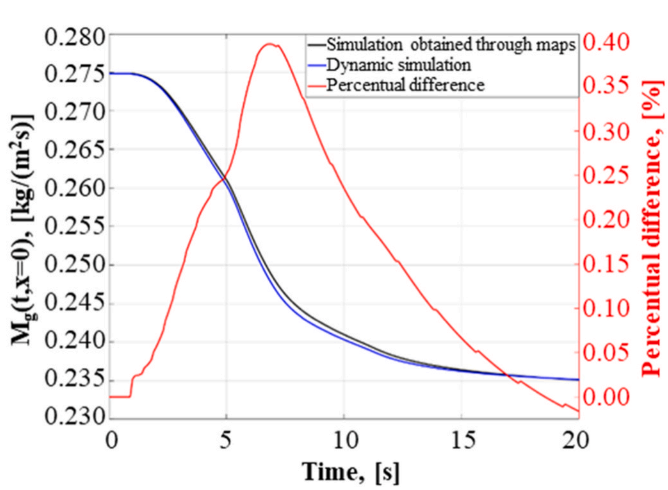

Fig. 7. Thermal protection material response to nozzle power variation at tail-off.

The blue line is computed solving the mathematical-physical model corresponding to material ablation with the above-mentioned trend of the nozzle radiating power. The percentual difference between the black and the blue line, computed as the percentual difference error with respect to the simulation obtained through maps, shows a maximum value of about 0.38 %. Such error means that the time scale needed for the thermal protection material to adapt to the new power condition is negligible if compared to the radiative power variation of the nozzle. Therefore, despite the fact that maps input parameters (h_c, T_{gas}, $\dot{Q}_{noz}$) are strongly time-dependent due to the unsteadiness of tail-off phase, steady-state thermal protection maps are assumed to be enough accurate in following tail-off fast variations of $\dot{Q}_{noz}$ in time. Even though $\dot{Q}_{noz}$ variation has been considered, it is important to state that variations in terms of h_c or T_{gas} have the same effect on char recession rate as the one given by $\dot{Q}_{noz}$, since those quantities are part of the thermal protection absorbed power (Eq. (16)). In conclusion, for the above-mentioned statements using a steady approximation regarding thermal protection material maps is allowed.

3.2. Thermal protections algorithm - ROBOOST integration procedure

The software used to analyze combustion chamber ballistics is *ROBOOST*, an in-house simulation environment originally developed to model SRM internal ballistics, including grain surface regression, combustion dynamics, and pressure/thrust time histories. It features a 3D surface regression module coupled with a 1D unsteady internal flow solver, allowing for the accurate modeling of grain anisotropy and combustion chamber fluid dynamics. In this work, *ROBOOST* was extended and integrated with a novel module for thermal protection ablation. It allows predicting each phase of *SRM* thrust performance, going from the ignition transient to tail-off. *ROBOOST* essentially consists of a *grain regression module* and a *ballistics* module. As far as the *grain regression module* is concerned, the general approach is based on 3D burning surface regression modelled as a 3D triangular mesh. An unstructured triangular mesh is applied, where the number of triangular elements relies on the trade-off between grain geometry shape

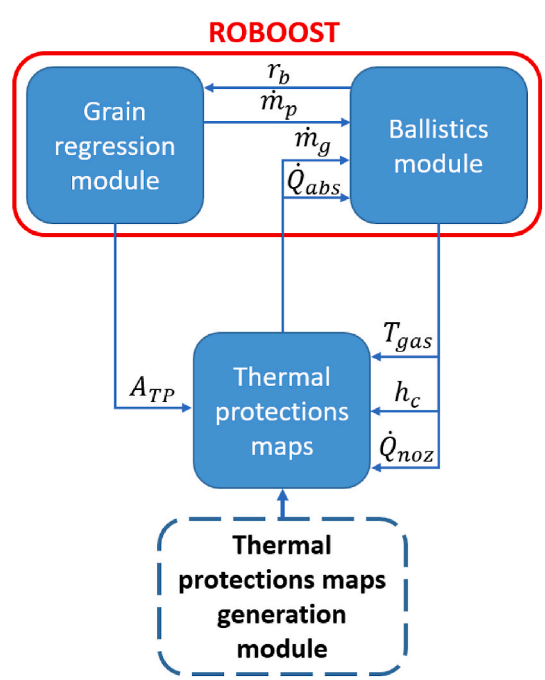

Fig. 8. Integration procedure scheme.

complexity and the desired degree of accuracy. Each mesh node is independently moved along the local unit-vector perpendicular to the discretized burning surface of a local displacement depending on the local burning rate. Such approach allows a point-by-point surface motion where each node is managed independently form the others, thus making the application of a variable burning rate depending on grain anisotropy possible. Moreover, in the direction of preserving mesh quality and coherence, a set of remeshing procedures has been established with the aim of handling maximum and minimum mesh size, triangle aspect ratio, and surface smoothing [45]. Since the motion of a 3D mesh can generate geometrical self-intersections, a mesh self-intersection removal algorithm has been integrated into *ROBOOST* software as a trade-off between the ability to handle generic geometrical shapes and computational effort. The above-mentioned procedure allows simulating the effect of defects such as air inclusions and propellant debonding into the grain. On the other hand, *ballistics module* relies on a 1D unsteady model [45] able to estimate the combustion chamber fluid dynamics along the *SRM* symmetry axis (z axis, Fig. 3). It is beyond the scope of this work to illustrate *ROBOOST* code in detail. A deeper *ROBOOST* explanation can be found in Ref. [45], which also includes the software validation with respect to *Z9 SRM* internal ballistics.

The integration of the thermal protection module represents a key innovation of the present work, enabling time-resolved simulation of post-burn-out thrust linked to thermal protection behavior. The original *ROBOOST* framework remains unchanged in terms of grain regression and core flow calculations, while this study provides a significant enhancement of its capabilities by incorporating the effects of ablative insulation and nozzle radiative feedback.

Fig. 8 shows the block diagram related to the connections between *ROBOOST* and the thermal protections maps.

The computational framework developed in this study involves several tightly coupled models and tools, each responsible for a specific aspect of the simulation. First, the NASA *CEA* program is used to compute the thermochemical properties of combustion gases (e.g., temperature, enthalpy, gas composition), which serve as inputs to both the thermal protection model and the *ROBOOST* internal ballistics module. The 1D thermal ablation model then uses these properties, along with convective heat transfer coefficients and nozzle radiative fluxes (computed from a nozzle temperature sub-model and geometric view factors), to generate multi-dimensional maps of pyrolysis gas mass flow rate and absorbed heat. These steady-state maps are imported into *ROBOOST*, which integrates them dynamically during the internal ballistic simulation. Then, combustion chamber pressure (and thrust) curve varying with time is carried out by solving the 1D fluid dynamics model coupled with those maps. At a certain time interval $\delta t = t - t_0$ of *ROBOOST* simulation, first the *grain regression module* estimates both the amount of burned propellant mass flow rate ($\dot{m}_p$) and the area (A_{TP}, Fig. 9a, where non-dimensional A_{TP} and non-dimensional time has been

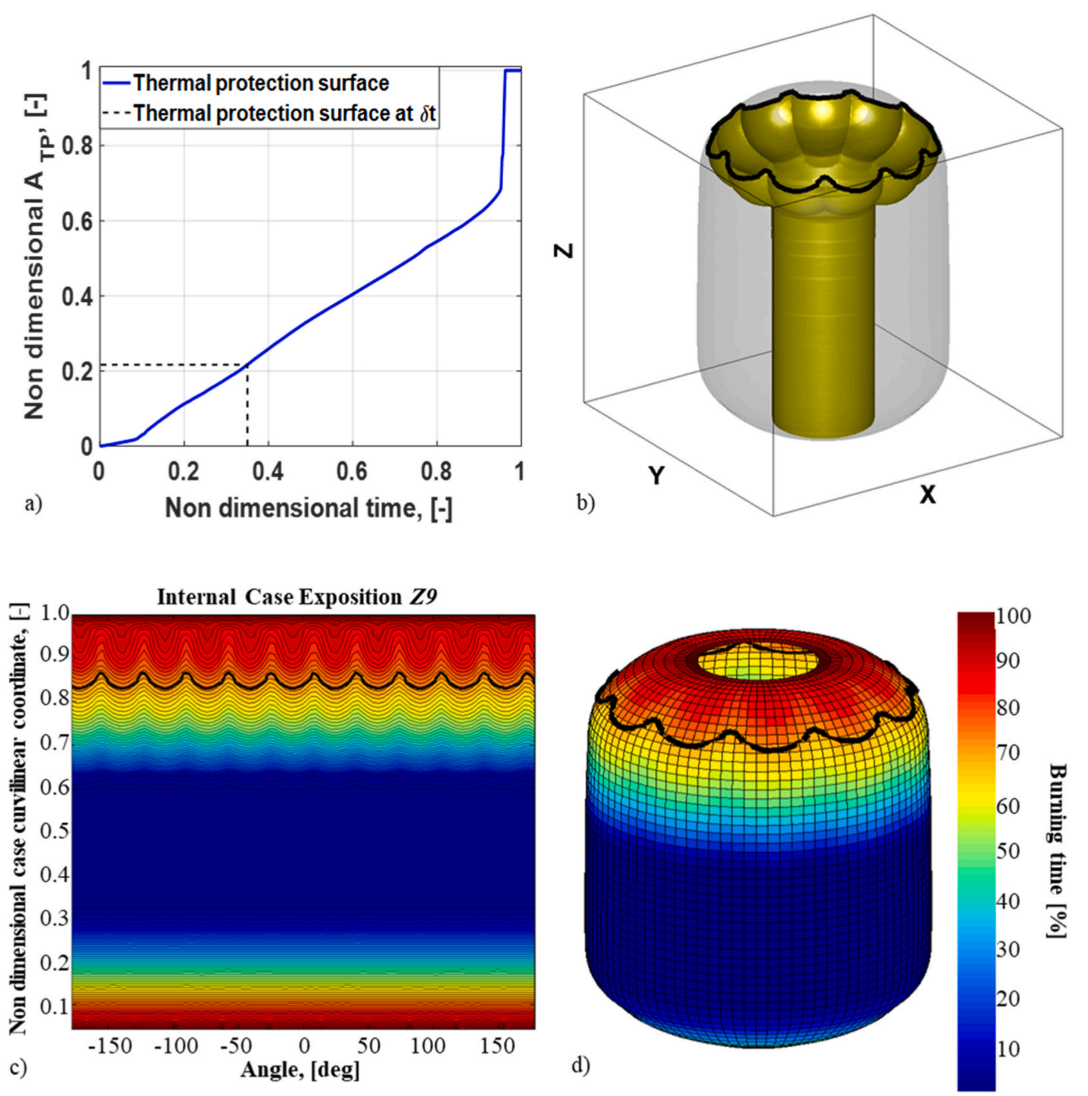

Fig. 9. *Z9* thermal protections exposition at Δt time interval.

computed by dividing each value respectively with the maximum value of A_{TP} and the maximum value of time) of thermal protections exposed to the combustion due to burning surface regression (Fig. 9b).

After that, the *ballistics module* computes a new propellant burning rate (r_b) from $\dot{m}_p$ and maps input quantities ($T_{gas}, h_c, \dot{Q}_{noz}$) using thermal protection mass flow rate ($\dot{m}_g$) and thermal protection absorbed power per unit surface ($\dot{Q}_{abs}$) belonging to the previous time instant t_0 as initial guess. Finally, the new burning rate estimation is used to compute a new value of $\dot{m}_p$ and A_{TP} with *grain regression module*. If the new values of both, $\dot{m}_p$ and A_{TP}, are below a fixed tolerance compared to those previously calculated, the algorithm moves forward to the next time iteration, otherwise the procedure is repeated until convergence is reached. Fig. 9c, d shows respectively the 2D and 3D thermal protections exposition map projected on *Z9* case in terms of percentage burning time. The case curvilinear coordinate is made non-dimensional through the curvilinear coordinate maximum value, whereas burning time is divided with respect to *Z9* burn-out time. The black dashed line marks the boundaries of the thermal protection region exposed to combustion at time δt.

Table 1
Input quantities.

Arrhenius equation parameters			
B $[1/s]$		$1.82{\cdot}10^4$	[49]
E_a $[J/mol]$		$4.66{\cdot}10^4$	[49]
ψ $[-]$		1	[49]
Virgin material properties			
ρ_v $[kg/m^3]$		1441.8	[49]
h_v^0 $[J/kg]$		$-1.4{\cdot}10^6$	[49]
T $[K]$	c_{p_v} $[J/(kg{\cdot}K)]$	k_v $[W/(m{\cdot}K)]$	[49]
300	1038	0.53	[49]
Char material properties			
ρ_c $[kg/m^3]$		961.2	[49]
h_c^0 $[J/kg]$		0	[49]
T $[K]$	c_{p_c} $[J/(kg{\cdot}K)]$	k_c $[W/(m{\cdot}K)]$	
370	1080	0.65	[49]
820	2235	1.94	[49]
Pyrolysis gas properties			
h_g^0 $[J/kg]$		0	[49]
c_{p_g} $[J/(kg{\cdot}K)]$		1660	[49]
Other parameters			
T_0 $[K]$		298.15	[49]
T_I $[K]$		293	
ε_{TP} $[-]$		0.8	[49]
α_s $[-]$		1	[44]
λ $[-]$		0.4	[31]
L $[m]$		0.01	
Constants			
R $[J/(mol{\cdot}K)]$		8.31	
σ $[W/(m^2{\cdot}K^4)]$		$5.67{\cdot}10^{-8}$	

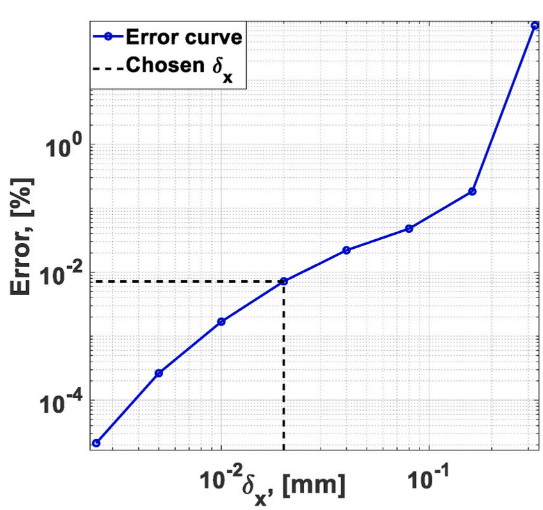

Fig. 10. Grid dependence analysis.

4. Results

Simulation results have been obtained on *Z9*. More specifically, *Z9* is marked out with a height of 3.5 m, a diameter of slightly less than 2 m, and a weight of 10.5 tons of *HTPB* based composite propellant. Its grain geometry consists of a circular cross section grain geometry in the fore and central parts, and fynocil-shaped configuration in the rear part near the nozzle inlet (Fig. 1). The ablative material used as thermal protection considered in this work is *X6300* characterized by a carbon-phenolic composition. Table 1 shows thermophysical properties of the thermal protection material (virgin and char material) and of the pyrolysis gases. Simulation domain length (L) of 0.01 m has been considered large enough to estimate the material behavior independently of the wall influence at $x = L$ (Fig. 4). T_I is the initial thermal protection material temperature before grain combustion starts, i.e., ambient temperature 293 K. Finally, R and σ are respectively the universal gas constant and the Stephan-Boltzmann constant. A linear interpolation has been considered for quantities varying with temperature; quantities specified for only one temperature value have been assumed constant.

The choice of the spatial step ($\delta x = 2{\cdot}10^{-2}$ mm, Fig. 10) is made in order to maintain the percentual convergence error lower than $7{\cdot}10^{-3}$ % . The percentual convergence error is computed as the percentual relative error between each value of $M_g(t, x = 0)$ corresponding respectively to each δx and the value of $M_g(t, x = 0)$ computed at a higher δx, namely $5{\cdot}10^{-4}$ mm. All results previously discussed have been obtained with *ROBOOST* software installed on a calculator with the following features: 16 Gb RAM, Intel Core i7-7th generation CPU machine with 3.10 GHz and NVIDIA Quadro M1200 graphic card. The generation process of the two maps lasted 48 h, while the internal ballistic simulation of *Z9* lasted 1 h.

Figs. 11 and 12 show respectively *X6300* maps without nozzle radiating and *X6300* maps with nozzle radiative contribution, considering the view factor equal to 0.09 (Fig. 6.). Time step and spatial step of the simulation performed to obtain the thermal protection maps (Figs. 11 and 12), are respectively $1{\cdot}10^{-4}$ s and $2{\cdot}10^{-2}$ mm., and maintained constant in order to numerically solve a uniform grid both in time and space. It is fundamental to highlight that the choice of time step is not relevant for the map usage in *ROBOOST*, but it has been conveniently determined to assess that map results are accurate enough.

Both presented maps belong to a larger set of maps, each one corresponding to different amounts of power radiated by the nozzle, as already explained in a previous section, and scaled with respect to its maximum value. Maps parameters, i.e., M_g, $T(t, x = 0)$, and power absorbed are scaled with respect to their maximum value. In order to consistently compare the two maps reported in Figs. 11 and 12, parameters maximum values are taken from the maps with nozzle radiation (Fig. 12). All of them are cubic interpolated within the ballistic simulation performed in *ROBOOST*. More specifically, the multi-dimensional interpolation process consists of interpolating a function of n independent variables at specific query points (points at which it is of interest knowing the value of the function) using cubic interpolation [50]. In the present work the n-dimensional function is represented by each one of the following maps computed at different nozzle radiation power: pyrolysis gases mass flow rate per unit surface M_g, free surface temperature $T(t, x = 0)$ and absorbed power $\dot{Q}_{abs}$. Each map relies on 3 independent variables, i.e., T_{gas}, h_c, and $\dot{Q}_{noz}$. Such values are estimated by *ROBOOST* internal ballistic model and, by using cubic interpolation, the query point of each map is identified.

Fig. 13 shows the percentual difference between the maps at both

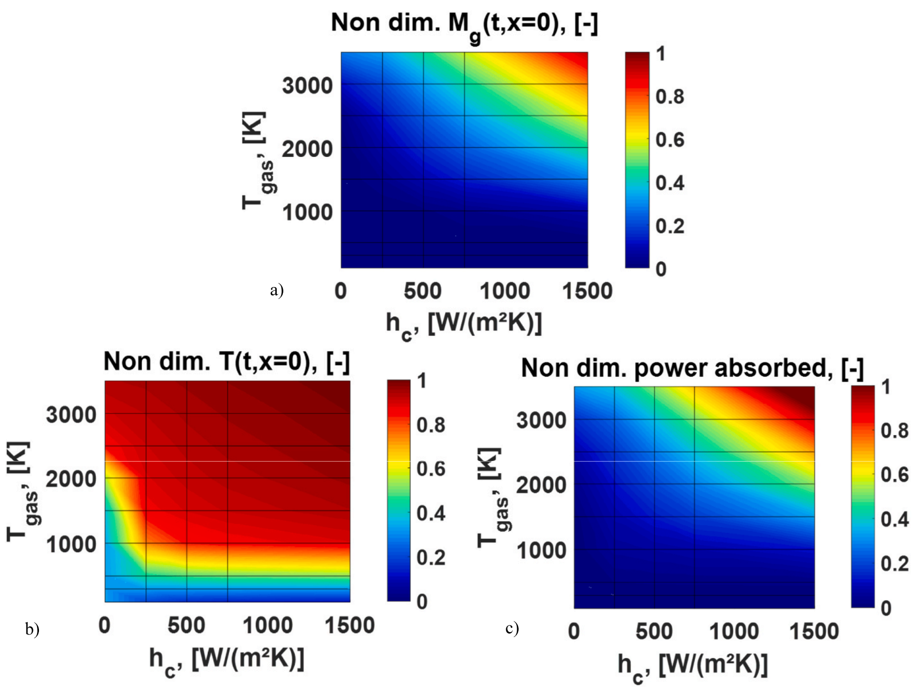

Fig. 11. *X6300* maps without nozzle radiation.

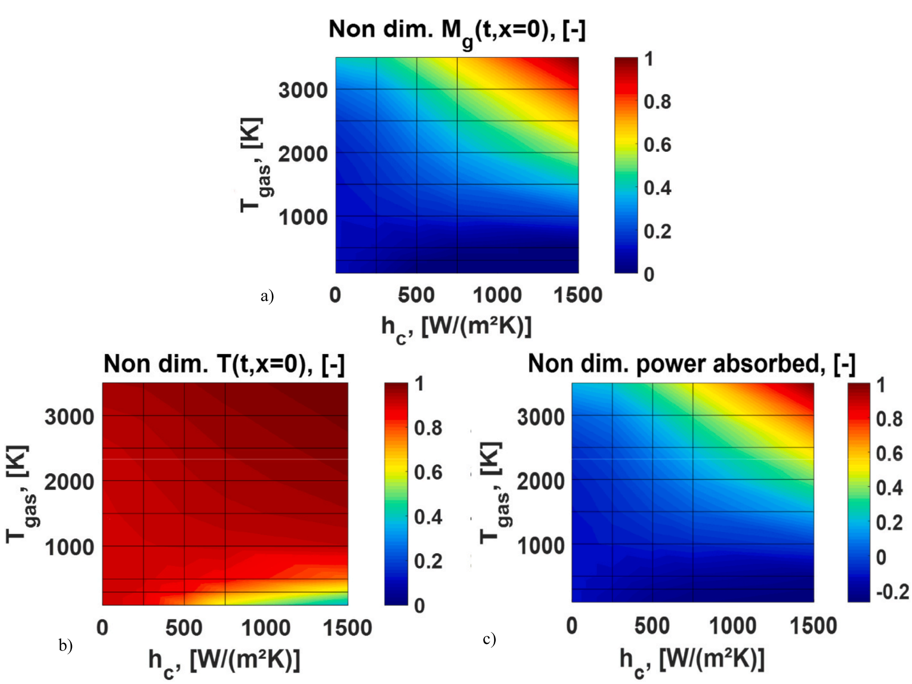

Fig. 12. *X6300* maps with nozzle radiation.

extremes, that is with and without nozzle radiation. The percentual difference of M_g, $T(t, x = 0)$ and the power absorbed have been computed as percentual relative difference with respect to the values included in the map without nozzle radiation (Fig. 11).

Some observations can be made on the presented maps. As expected, ablation caused by combustion chamber hot gases thermal convection together with nozzle radiation has a higher intensity with respect to ablation without nozzle radiation. As a matter of fact, as shown in Fig. 13a and b, the average increment of char recession rate and pyrolysis gas mass flow rate per unit surface due to additional amount of heat coming from the nozzle is close to 10 %. More precisely, such increment is higher for h_c close to zero. In fact, null heat transfer convective coefficient corresponds to the condition of the combustion chamber where grain combustion is over and hot gases velocity is nearly equal to zero since all combustion gases almost left combustion chamber. Thus, hot gas convection does not occur anymore and nozzle radiation is the only effect sustaining thermal protection ablation in those conditions. The above-mentioned statement can be proven comparing, for instance, Figs. 11a and 12a at $h_c = 0$ and $T_{gas} < 2000\,K$: Fig. 11a recession rate is substantially lower than Fig. 12a recession rate. That is also confirmed considering Fig. 11c where the low pyrolysis gas temperature means that ablation process is almost absent while the contrary

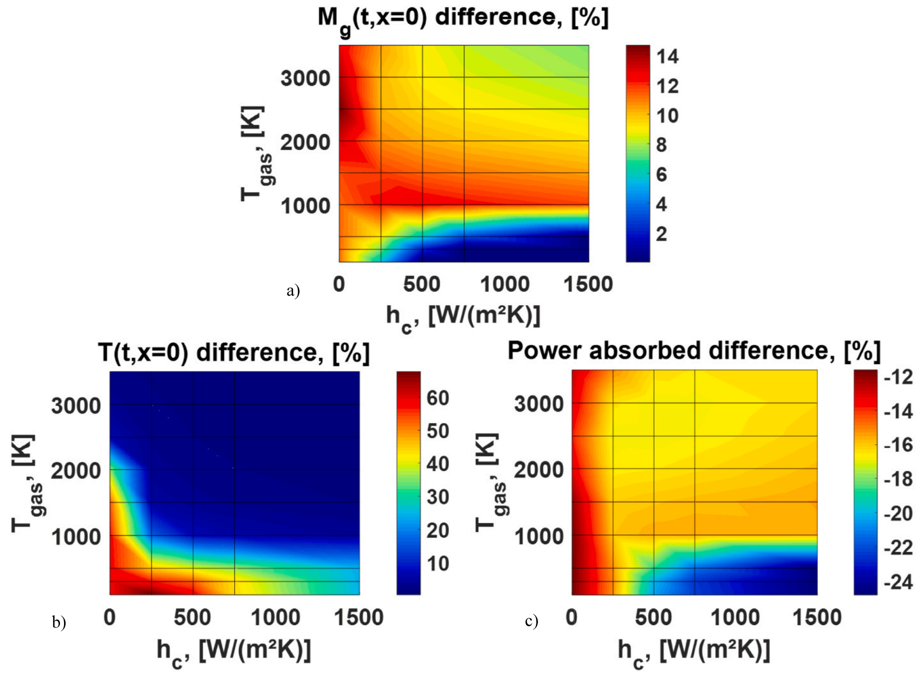

Fig. 13. Difference between *X6300* map without nozzle contribution and *X6300* map with nozzle contribution.

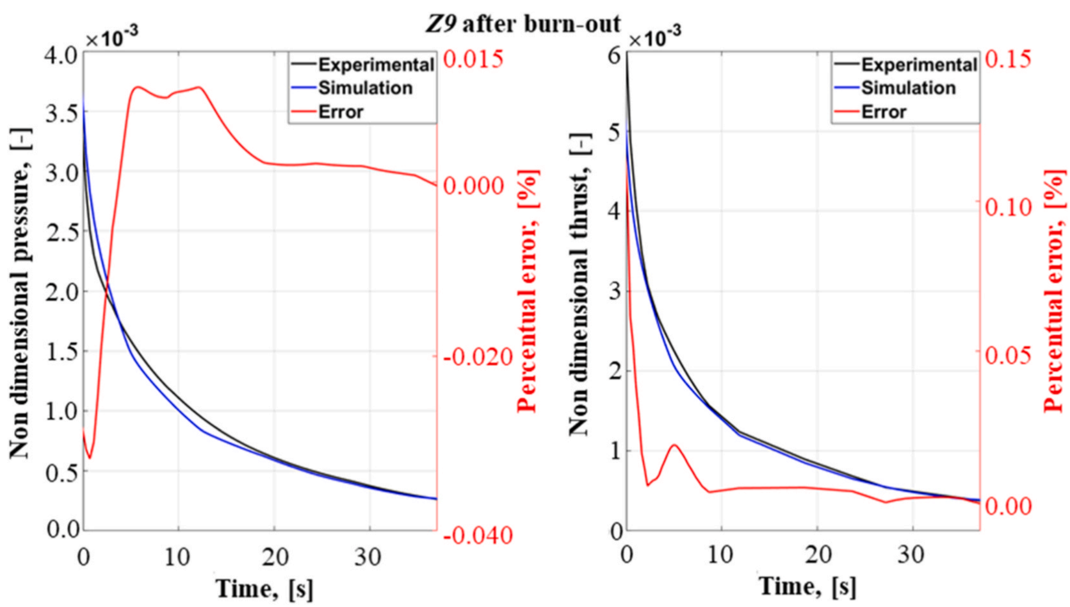

Fig. 14. *Z9* residual pressure and thrust.

happens in Fig. 12c. This is shown even more clearly in Fig. 13. In fact, the maximum difference in terms of char recession rate and pyrolysis gas mass flow rate per unit surface (Fig. 13a and b) is located at h_c close to zero, meaning that the nozzle radiative power has a fundamental role at burn-out when grain combustion is over.

The negative value reached by the absorbed power in Fig. 13c is also worth mentioning. As stated before, absorbed power represents only the amount of power exchanged between thermal protections and combustion chamber hot gases; when the nozzle is radiating, the power absorbed from hot gases is lower due to additional amounts of heat coming from the nozzle itself that causes an increase in thermal protection temperature. If the nozzle radiation is strong and the gas temperature is low (see Fig. 12a,b,c in the interval $T_{gas} < 500\ K$ and $h_c > 500\ W/_{m^2K}$), it may occur that the temperature reached by the thermal protection is higher than T_{gas} and, for this reason, heat exchange takes place in the opposite direction, thus justifying the negative value. It is clear that such condition is an extreme case that occurs only when propellant combustion is complete and the nozzle is still hot, for instance, after tail-off.

The red region in Fig. 13c emphasizes the earlier achievement of ablation temperature by thermal protection with nozzle radiating without nozzle effect, justifying the higher char recession rate.

After importing these maps into the simulation software, the final step is the internal ballistics simulation.

Z9 pressure/thrust prediction has been obtained by including in *ROBOOST* internal ballistics module the maps obtained from the quantities shown in Table 1 (regarding the thermochemical properties of thermal protection material) and two constants K_1 and K_2 (respectively

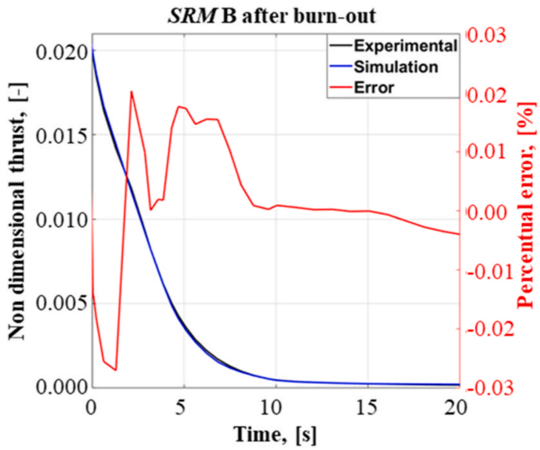

Fig. 15. *SRM* B residual thrust.

equal to $3 \cdot 10^{-6}\ \frac{m^2K}{W}$ and 0.5 and included in the char mechanical erosion model, Eq. (17)).

Fig. 14 shows a comparison between experimental and simulated trends in terms of *Z9* combustion chamber residual pressure and residual thrust after burn-out. Non dimensional pressure and thrust have been computed by dividing each value by respectively the maximum pressure and thrust linked to the experimental data. Moreover, the percentual error has been evaluated as the relative percentual error with respect to the experimental curves. Pressure maximum error (absolute value) is 0.03 %, while thrust error is nearly 0.12 % which means that there is an acceptable match between simulation and experimental data. As it can be noticed, internal pressure (and therefore thrust) lasts for tens of seconds after burn-out and pressure levels are such that they can be usually considered negligible with respect to ambient pressure for first stage motors. This does not apply to *Z9* since being a third stage means that outside pressure is almost negligible and, in addition, the total impulse produced after burn-out acts on a small residual mass, thus generating non negligible accelerations. For this reason, the ability to predict such residual thrust is fundamental to properly design the separation procedure, both in terms of timings and separation motors total impulse. In the direction of proving the predictive ability of the above-mentioned procedure, another upper stage solid rocket motor, namely *SRM* B, has been examined. Since *SRM* B has a different case size and nozzle geometry while having the same *HTPB*-based composite propellant and thermal protection material as *Z9*, maps parameters considered for *SRM* B residual thrust simulation are the same as the ones employed in *Z9* thrust prediction, except for the view factor distribution. In fact, such quantity is different with respect to *Z9* view factor because it depends on how the surface of the thermal protection case is hit by nozzle radiative power. This means that both nozzle and case geometry have an impact in predicting residual thrust behavior, however, they are determined by the motor shape.

The result of the simulation for the second motor is shown in Fig. 15, where the thrust has been normalized by *SRM* B maximum thrust and the percentual error is computed as the percentual relative error with respect to the experimental data. A maximum error of 0.027 % occurs which means that the result of the *SRM* B simulation can be considered satisfactory. Since the residual thrust-estimation procedure has been successfully applied to two *SRM* configurations by using the same suitable parameters of *Z9* except for the view factor, the method proposed can be recognized as predictive.

The proposed model is developed with a modular approach, allowing its adaptation to different thermal protection materials and nozzle configurations. Given that ablation behavior and pyrolysis gas generation are highly dependent on material composition, the model requires appropriate input parameters specific to the thermal protection material in use, such as thermal conductivity, density, specific heat, and degradation kinetics. If these parameters are well-characterized, the model can be extended to other ablative materials with reasonable accuracy. Furthermore, since nozzle structure and composition influence radiative heat transfer, the model incorporates view factors and radiative flux estimates that can be adjusted for different nozzle geometries. However, its applicability is best suited to configurations where the primary residual thrust source is pyrolysis gas expansion. For cases with significant contributions from molten slag or other combustion byproducts, additional refinements may be necessary. Future work could focus on refining the model's predictive capability for a broader range of materials and propulsion systems.

5. Conclusion

A physical-numerical procedure has been proposed to predict the effect of thermal protections insulation layer on tail-off phase of *Z9* internal ballistic performance. First, a map generating procedure has been carried out using finite difference numerical technique. The main outcome is that nozzle radiation during tail-off seems to be the key factor in sustaining material ablation after *SRM* burn-out. Then, the above-mentioned maps were given as input to an in-house developed software in order to predict residual combustion chamber pressure and thrust - time profile. A quite appreciable percentage relative error is obtained regarding the comparisn with the experimental trend. Moreover, residual thrust of a second motor has been estimated with the aim of proving the predictive ability of the entire procedure.

Simulation results indicate that residual thrust persists for at least 20–30 s after propellant burnout, with a peak value of 0.5 % of the nominal thrust level. Comparison with experimental data for *Z9* showed a maximum deviation of 0.12 % in predicted thrust and 0.03 % in pressure, confirming the model's accuracy.

Additionally, the model was applied to a second *SRM* configuration (*SRM* B) with different nozzle geometry but identical thermal protection material. The simulated residual thrust trend closely matched experimental results, with a maximum prediction error of 0.027 %, validating the model's predictive capability across different configurations. These findings suggest that the methodology can be extended to other *SRM* designs, provided that material properties and nozzle radiative characteristics are well-characterized.

CRediT authorship contribution statement

F. Ponti: Writing – review & editing, Validation, Supervision, Project administration, Methodology, Investigation, Formal analysis, Conceptualization. **S. Mini:** Writing – review & editing, Writing – original draft, Validation, Methodology, Investigation, Formal analysis, Data curation, Conceptualization. **V. Ravaglioli:** Writing – review & editing, Supervision, Methodology. **A. Annovazzi:** Visualization, Validation, Supervision, Project administration, Methodology, Investigation, Funding acquisition, Formal analysis, Data curation, Conceptualization. **M. Fiorillo:** Supervision, Funding acquisition. **E. Gizzi:** Validation, Supervision, Methodology, Conceptualization.

Declaration of competing interest

The authors declare that they have no known competing financial interests or personal relationships that could have appeared to influence the work reported in this paper.

Appendix A

The derivation presented here follows the classical framework for treating mass and energy balances in a regressing condensed phase, as extensively discussed in the literature (e.g., Culick's foundational review on unsteady solid propellant burning [51]). For completeness, the governing conservation equations for mass, momentum, and energy are restated, and then adapted to the specific case of charring ablative thermal protection materials.

The main novelty of this derivation lies in the treatment of the pyrolysis gas mass flow and the coupling between char density variation and thermal conduction within the ablative layer. Unlike propellant regression, where the gas generation rate is primarily linked to surface burning, here the decomposition of virgin material into char and pyrolysis gases requires inclusion of in-depth energy balances and Arrhenius-type decomposition kinetics.

Fig. 16 shows an infinitesimal element of thermal protection material whose free surface recedes from point O' to point O with $\dot{s}$ as recession rate. The space covered between O' and O is named s and it depends on time θ (or t). Two reference frames are established. The first one is tied to the initial position of the free surface, i.e., O' and it is identified by the spatial coordinate y; while the second one is attached to the free surface (point O in Fig. 16) and it relies on the spatial coordinate x. First, an energy-balance equation is considered with respect to the fixed reference frame. Moreover, some assumptions are established in the direction of obtaining the mathematical relation (Eq. (30)). Thermal conduction is considered 1D along y axis (or x axis) (Fig. 16). Any pysolisis gases formed during pyrolisis phenomenon are in thermal equilibrium with char and do no react chemically with the char itself. Moreover, pyrolsis gases are assumed to pass immediately out through the char implying a zero residence time.

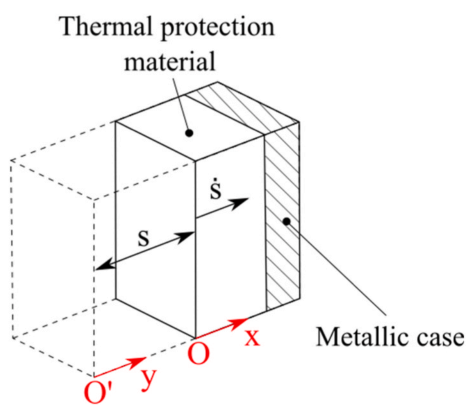

Fig. 16. Thermal protection control volume at a generic time instant.

The 1D energy differential equation [31] expressed in terms of the spatial coordinate y (located at the free surface of thermal protection material before the pyrolysis has started) and the temporal coordinate θ is shown through Eq. (30)

$$\frac{\partial(\rho HA)}{\partial\theta} = \frac{\partial}{\partial y}\left(kA\frac{\partial T}{\partial y}\right) + \frac{\partial(\dot{m}_g H_g)}{\partial y} \tag{30}$$

$\frac{\partial(\rho HA)}{\partial\theta}$ represents the energy storage term, $\frac{\partial}{\partial y}\left(kA\frac{\partial T}{\partial y}\right)$ identifies the heat conduction, and $\frac{\partial(\dot{m}_g H_g)}{\partial y}$ serves as the heat convection due to pyrolysis gases exiting the char layer.

By considering the thermal protection cross-section surface A not depending on y (or x) meaning that such surface remains constant along the spatial coordinate, Eq. (30) can be rewritten into the relation expressed by Eq. (31).

$$\frac{\partial(\rho H)}{\partial\theta} = \frac{\partial}{\partial y}\left(k\frac{\partial T}{\partial y}\right) + \frac{\partial(M_g H_g)}{\partial y} \tag{31}$$

where M_g replaces the quantity $\dot{m}_g/A$

For the numerical solution it is convenient to consider the moving reference frame fixed to the receding surface (x coordinate in Figure 16). In fact, it is preferable to drop spatial grid nodes from the non-ablating surface (thermal protection material surface next to the metallic case in Figure 16) than from the char receding surface (cross-section surface crossing point O' in Figure 16). Therefore, the following coordinate conversion relations (Eq. (32)) are involved to switch from the fixed coordinate reference frame (θ, y) to the moving coordinate reference frame (t, x).

$$\begin{cases} t = \theta \\ x = y - s \end{cases} \tag{32}$$

where s is a function of time θ.

The partial derivative conversion formulas obtained with Eq. (32) are:

$$\begin{cases} \dfrac{\partial(\dots)}{\partial\theta} = \dfrac{\partial(\dots)}{\partial t} - \dot{s}\dfrac{\partial(\dots)}{\partial x} \\ \dfrac{\partial(\dots)}{\partial y} = \dfrac{\partial(\dots)}{\partial x} \end{cases} \tag{33}$$

where $\dot{s} = \frac{ds}{d\theta}$

Applying Eq. (32) to Eq. (30) yields:

$$\frac{\partial(\rho H)}{\partial t} = \frac{\partial}{\partial x}\left(k\frac{\partial T}{\partial x}\right) + \dot{s}\frac{\partial(\rho H)}{\partial x} + \frac{\partial(M_g H_g)}{\partial x} \tag{34}$$

Let identify each term $\frac{\partial(\rho H)}{\partial t}$, $\frac{\partial}{\partial x}\left(k\frac{\partial T}{\partial x}\right)$, $\dot{s}\frac{\partial(\rho H)}{\partial x}$, $\frac{\partial(M_g H_g)}{\partial x}$ respectively with *Term 1*, *Term 2*, *Term 3*, *Term 4*. Regarding *Term 1*, it is convenient to express the partially pyrolyzed material as a mixture of pure char and pure virgin material. It is assumed that Ω_v represents the volume fraction of virgin material in the control volume. For undecomposed material $\Omega_v = 1$, for pure char material $\Omega_v = 0$ [31]. Material density and enthalpy are expressed as weighted averages of virgin and char fractions, following the standard procedure, yielding the final form of *Term 1* as:

$$\frac{\partial(\rho H)}{\partial t} = \frac{\rho_v H_v - \rho_c H_c}{\rho_v - \rho_c}\frac{\partial \rho}{\partial t} + \left[\rho\left(\frac{\rho_v c_{p_v} - \rho_c c_{p_c}}{\rho_v - \rho_c}\right) - \frac{\rho_v \rho_c}{\rho_v - \rho_c}\left(c_{p_v} - c_{p_c}\right)\right]\frac{\partial T}{\partial t} \tag{35}$$

Introducing the following definitions:

$$\overline{H} = \frac{\rho_v H_v - \rho_c H_c}{\rho_v - \rho_c}, \alpha = \frac{\rho_v c_{p_v} - \rho_c c_{p_c}}{\rho_v - \rho_c}, \beta = \frac{\rho_v \rho_c}{\rho_v - \rho_c}\left(c_{p_v} - c_{p_c}\right) \tag{36}$$

Eq. (35) may be written as follows (Eq. (37)):

$$\frac{\partial(\rho H)}{\partial t} = \overline{H}\frac{\partial \rho}{\partial t} + (\alpha\rho - \beta)\frac{\partial T}{\partial t} \tag{37}$$

Moreover, it is possible to prove [31] that the link between virgin material mass fraction X and volume fraction is (Eq. (38)):

$$\mathrm{X} = \frac{\Omega_v \rho_v}{\rho} = \frac{\rho_v}{\rho_v - \rho_c}\left(1 - \frac{\rho_c}{\rho}\right) \tag{38}$$

Within the partially pyrolyzed material, the heat thermal conductivity is formulated as the mean weighted average between the mass fraction of virgin material X and the mass fraction of char material $1 - \mathrm{X}$. (Eq. (39)).

$$\mathrm{k} = \mathrm{X}k_v + (1 - \mathrm{X})k_c \tag{39}$$

Substituting Eq. (38) and Eq. (39) into *Term 2*, i.e., $\frac{\partial}{\partial x}\left(k\frac{\partial T}{\partial x}\right)$, Eq. (40) is established:

$$\frac{\partial}{\partial x}\left(k\frac{\partial T}{\partial x}\right) = \left[(k_v - k_c)\frac{\rho_v \rho_c}{\rho_v - \rho_c}\frac{1}{\rho^2}\frac{\partial \rho}{\partial x} + \frac{\rho_v}{\rho_v - \rho_c}\left(1 - \frac{\rho_c}{\rho}\right)\left(\frac{\partial k_v}{\partial x} - \frac{\partial k_c}{\partial x}\right) + \frac{\partial k_c}{\partial x}\right]\frac{\partial T}{\partial x} + \left[\frac{\rho_v k_v - \rho_c k_c}{\rho_v - \rho_c} - \frac{1}{\rho}\frac{\rho_v \rho_c}{\rho_v - \rho_c}(k_v - k_c)\right]\frac{\partial^2 T}{\partial x^2} \tag{40}$$

The following definitions are introduced:

$$\eta = \frac{\rho_v k_v - \rho_c k_c}{\rho_v - \rho_c}, \xi = \frac{\rho_v \rho_c}{\rho_v - \rho_c}(k_v - k_c) \tag{41}$$

With Eq.s (41), Eq. (40) is rearranged into Eq. (42):

$$\frac{\partial}{\partial x}\left(k\frac{\partial T}{\partial x}\right) = \left[\frac{\xi}{\rho^2}\frac{\partial \rho}{\partial x} + \frac{\rho_v}{\rho_v - \rho_c}\left(1 - \frac{\rho_c}{\rho}\right)\left(\frac{\partial k_v}{\partial x} - \frac{\partial k_c}{\partial x}\right) + \frac{\partial k_c}{\partial x}\right]\frac{\partial T}{\partial x} + \left(\eta - \frac{\xi}{\rho}\right)\frac{\partial^2 T}{\partial x^2} \tag{42}$$

Since $\frac{\partial k_v}{\partial x} = \frac{dk_v}{dT}\frac{\partial T}{\partial x}$ and $\frac{\partial k_c}{\partial x} = \frac{dk_c}{dT}\frac{\partial T}{\partial x}$, Eq. (43) may be rewritten into Eq. (43), representing the final form of *Term 2*.

$$\frac{\partial}{\partial x}\left(k\frac{\partial T}{\partial x}\right) = \left[\frac{\xi}{\rho^2}\frac{\partial \rho}{\partial x} + \left(\frac{\rho_v}{\rho_v - \rho_c}\left(1 - \frac{\rho_c}{\rho}\right)\left(\frac{dk_v}{dT} - \frac{dk_c}{dT}\right) + \frac{dk_c}{dT}\right)\frac{\partial T}{\partial x}\right]\frac{\partial T}{\partial x} + \left(\eta - \frac{\xi}{\rho}\right)\frac{\partial^2 T}{\partial x^2} \tag{43}$$

Term 3 may be written in a similar way to *Term 1* (Eq. (37)), considering the application of $\frac{\partial(\dots)}{\partial x}$ to ρH instead of $\frac{\partial(\dots)}{\partial t}$ (Eq. (44)).

$$\dot{s}\frac{\partial(\rho H)}{\partial x} = \overline{H}\dot{s}\frac{\partial \rho}{\partial x} + \dot{s}(\alpha\rho - \beta)\frac{\partial T}{\partial x} \tag{44}$$

Finally, *Term 4* is written as follows (Eq. (45)):

$$\frac{\partial(M_g H_g)}{\partial x} = H_g\frac{\partial M_g}{\partial x} + M_g c_{p_g}\frac{\partial T}{\partial x} \tag{45}$$

Substituting Eqs. (37) and (43)–(45) into Eq. (34), Eq. (46) is established:

$$(\alpha\rho - \beta)\frac{\partial T}{\partial t} = \left[\frac{\xi}{\rho^2}\frac{\partial \rho}{\partial x} + \left(\frac{\rho_v}{\rho_v - \rho_c}\left(1 - \frac{\rho_c}{\rho}\right)\left(\frac{\partial k_v}{\partial x} - \frac{\partial k_c}{\partial x}\right) + \frac{\partial k_c}{\partial x}\right)\frac{\partial T}{\partial x}\right]\frac{\partial T}{\partial x} + \left(\eta - \frac{\xi}{\rho}\right)\frac{\partial^2 T}{\partial x^2} + \overline{H}\dot{s}\frac{\partial \rho}{\partial x} - \overline{H}\frac{\partial \rho}{\partial t} + \dot{s}(\alpha\rho - \beta)\frac{\partial T}{\partial x} + H_g\frac{\partial M_g}{\partial x} + M_g c_{p_g}\frac{\partial T}{\partial x} \tag{46}$$

Since total mass conservation among virgin material, char material and pyrolysis gases is carried out [31], Eq. (46) can be rearranged in the following way (Eq. (47)):

$$(\alpha\rho - \beta)\frac{\partial T}{\partial t} = \left(H_g - \overline{H}\right)\frac{\partial M_g}{\partial x} + \left[\dot{s}(\alpha\rho - \beta) + M_g c_{p_g} + \frac{\xi}{\rho^2}\frac{\partial \rho}{\partial x} + \left(\frac{\rho_v}{\rho_v - \rho_c}\left(1 - \frac{\rho_c}{\rho}\right)\left(\frac{dk_v}{dT} - \frac{dk_c}{dT}\right) + \frac{dk_c}{dT}\right)\frac{\partial T}{\partial x}\right]\frac{\partial T}{\partial x} + \left(\eta - \frac{\xi}{\rho}\right)\frac{\partial^2 T}{\partial x^2} \tag{47}$$

By dividing both the left-hand side and the right-hand side term of Eq. (47) by the quantity $(\alpha\rho - \beta)$, Eq. (3) is proven.

References

[1] S. Boraas, B. Hyland, L. Smart, Predicted post burn residual thrust for an orbital transfer motor, in: 21st Joint Propulsion Conference, American Institute of Aeronautics and Astronautics, Reston, Virigina, 1985, https://doi.org/10.2514/6.1985-1395.
[2] R. Akiba, M. Kohno, Experiments with solid rocket technology in the development of M-3SII, Acta Astronaut. 13 (1986) 349–361, https://doi.org/10.1016/0094-5765(86)90090-1.
[3] W.A. Johnston, J.W. Murdock, S. Koshigoe, P.T. Than, Slag accumulation in the Titan solid rocket motor upgrade, J. Propul. Power 11 (1995) 1012–1020, https://doi.org/10.2514/3.23931.
[4] R.X. Meyer, In-flight formation of slag in spinning solid propellant rocket motors, J. Propul. Power 8 (1992) 45–50, https://doi.org/10.2514/3.23440.
[5] C. JasperLal, P. Sridharan, K. Krishnaraj, V. Srinivasan, Investigation of slag accumulation in solid rocket motors, in: 49th AIAA/ASME/SAE/ASEE Joint Propulsion Conference, American Institute of Aeronautics and Astronautics, Reston, Virginia, 2013, https://doi.org/10.2514/6.2013-3861.
[6] B. Toth, M.R. Lema, P. Rambaud, J. Anthoine, J. Steelant, Assessment of slag accumulation in solid Rocket boosters: summary of the VKI research, in: 43rd AIAA/ASME/SAE/ASEE Joint Propulsion Conference & Exhibit, American Institute of Aeronautics and Astronautics, Reston, Virigina, 2007, https://doi.org/10.2514/6.2007-5760.
[7] V.E. Haloulakos, Slag mass accumulation in spinning solid rocket motors, J. Propul. Power 7 (1991) 14–21, https://doi.org/10.2514/3.23288.
[8] I.-S. Chang, Slag and thermal environment of a spinning rocket motor, J. Spacecraft Rockets 28 (1991) 599–605, https://doi.org/10.2514/3.26286.
[9] J.K. Sambamurthi, A. Alvarado, E.C. Mathias, Correlation of slag expulsion with ballistic anomalies in shuttle solid rocket motors, J. Propul. Power 12 (1996) 625–631, https://doi.org/10.2514/3.24082.
[10] K.W. Dotson, J.W. Murdock, D.K. Kamimoto, Launch vehicle dynamic and control effects from solid rocket motor slag ejection, J. Propul. Power 15 (1999) 468–475, https://doi.org/10.2514/2.5450.
[11] Y. Matsuura, K. Nitta, H. Ikeda, M. Kinoshita, K. Ui, Evaluation of the material properties of solid rocket motor slag, IOP Conf. Ser. Mater. Sci. Eng. 1287 (2023) 012005, https://doi.org/10.1088/1757-899X/1287/1/012005.
[12] Y. Guan, J. Li, Y. Liu, N. Yan, Deposits evolution and its heat transfer characteristics research in solid rocket motor, Appl. Therm. Eng. 184 (2021) 116266, https://doi.org/10.1016/j.applthermaleng.2020.116266.
[13] P.R.M. Panicker, N. Ramachandran, K.P. Sreekumar, M.R.A. Majeed, Pyrolysis caused tail-off thrust in a solid rocket motor: a semi-empirical model, Def. Sci. J. 48 (1998) 87–91, https://doi.org/10.14429/dsj.48.3870.
[14] J. Wang, N. Wang, X. Zou, W. Dong, C. Wang, L. Han, B. Shi, Experimental and numerical study on slag deposition in solid rocket motor, Aero. Sci. Technol. 122 (2022) 107404, https://doi.org/10.1016/j.ast.2022.107404.
[15] D. Schiariti, F. Paglia, E. Gizzi, C. Milana, D. Barbagallo, A. Neri, Prediction of the residual thrust of 2nd and 3rd Vega Launcher Solid Rocket Motors stages after the burn-out, due to internal thermal protection pyrolysis, in: 7TH EUROPEAN CONFERENCE FOR AERONAUTICS AND SPACE SCIENCES, EUCASS), Milan, 2017.
[16] Y. Guan, J. Li, Y. Liu, T. Xu, Influence of different propellant systems on ablation of EPDM insulators in overload state, Acta Astronaut. 145 (2018) 141–152, https://doi.org/10.1016/j.actaastro.2018.01.048.
[17] T.P. Kibbey, Residual thrust in a solid rocket motor: a model applied to the Mars ascent vehicle, in: AIAA SCITECH 2024 Forum, American Institute of Aeronautics and Astronautics, Reston, Virginia, 2024, https://doi.org/10.2514/6.2024-0212.
[18] J. Koo, W. Ho, O. Ezekoye, A review of ablation modeling for thermal protection systems, in: 42nd AIAA/ASME/SAE/ASEE Joint Propulsion Conference & Exhibit, American Institute of Aeronautics and Astronautics, Reston, Virigina, 2006, https://doi.org/10.2514/6.2006-4936.
[19] P.G. Cross, I.D. Boyd, Two-Dimensional modeling of ablation and pyrolysis with application to rocket nozzles, J. Spacecraft Rockets 54 (2017) 212–224, https://doi.org/10.2514/1.A33656.
[20] Z. Ma, Z. Wei, Y. Feng, C. Wang, W. Dong, N. Wang, B. Shi, Experimental study on the collision behaviors of micron-sized aluminum droplets with solid wall in high temperature burned gas, Aero. Sci. Technol. 115 (2021) 106791, https://doi.org/10.1016/j.ast.2021.106791.
[21] F. Ponti, S. Mini, L. Fadigati, V. Ravaglioli, A. Annovazzi, V. Garreffa, Effects of inclusions on the performance of a solid rocket motor, Acta Astronaut. 189 (2021) 283–297, https://doi.org/10.1016/j.actaastro.2021.08.030.
[22] S. Mini, F. Ponti, A. Brusa, R. Bertacin, B. Betti, Prediction of tail-off pressure peak Anomaly on small-scale rocket motors, Aerospace 10 (2023) 169, https://doi.org/10.3390/aerospace10020169.
[23] M.B. Dow, R.T. Swann, S.S. Tompkins, Analysis of the effects of environmental conditions on the performance of charring ablators, J. Spacecraft Rockets 3 (1966) 61–67, https://doi.org/10.2514/3.28386.
[24] M.L. Blosser, Fundamental modeling and thermal performance issues for metallic thermal protection System concept, J. Spacecraft Rockets 41 (2004) 195–206, https://doi.org/10.2514/1.9182.
[25] A.R. Bahramian, M. Kokabi, M.H.N. Famili, M.H. Beheshty, Ablation and thermal degradation behaviour of a composite based on resol type phenolic resin: process modeling and experimental, Polymer (Guildf.) 47 (2006) 3661–3673, https://doi.org/10.1016/j.polymer.2006.03.049.
[26] W. Li, H. Huang, Y. Tian, Z. Zhao, A nonlinear pyrolysis layer model for analyzing thermal behavior of charring ablator, Int. J. Therm. Sci. 98 (2015) 104–112, https://doi.org/10.1016/j.ijthermalsci.2015.07.002.
[27] A.J. Amar, B.F. Blackwell, J.R. Edwards, One-dimensional ablation using a full newton's method and finite control volume procedure, J. Thermophys. Heat Tran. 22 (2008) 71–82, https://doi.org/10.2514/1.29610.
[28] A.J. Amar, B.F. Blackwell, J.R. Edwards, Development and verification of a one-dimensional ablation code including pyrolysis gas flow, J. Thermophys. Heat Tran. 23 (2009) 59–71, https://doi.org/10.2514/1.36882.
[29] H. Mohammadiun, M. Mohammadiun, Numerical modeling of charring material ablation with considering chemical-reaction effects, mass transfer and surface heat transfer, Arabian J. Sci. Eng. 38 (2013) 2533–2543, https://doi.org/10.1007/s13369-012-0510-0.
[30] M.A. Covington, J.M. Heinemann, H.E. Goldstein, Y.-K. Chen, I. Terrazas-Salinas, J. A. Balboni, J. Olejniczak, E.R. Martinez, Performance of a low density ablative heat shield material, J. Spacecraft Rockets 45 (2008) 237–247, https://doi.org/10.2514/1.12403.
[31] R.J. Schoner, User's Manual Aerotherm Charring Material Thermal Response and Ablation Program, 1970.
[32] Y.-K. Chen, F.S. Milos, Ablation and thermal response Program for spacecraft heatshield analysis, J. Spacecraft Rockets 36 (1999) 475–483, https://doi.org/10.2514/2.3469.
[33] F.S. Milos, Y.-K. Chen, Ablation, Thermal Response, and Chemistry Program for analysis of thermal protection systems, J. Spacecraft Rockets 50 (2013) 137–149, https://doi.org/10.2514/1.A32302.
[34] F.S. Milos, Y.-K. Chen, Ablation and thermal response property model validation for phenolic impregnated carbon ablator, J. Spacecraft Rockets 47 (2010) 786–805, https://doi.org/10.2514/1.42949.
[35] J. Lachaud, T. van Eekelen, J.B. Scoggins, T.E. Magin, N.N. Mansour, Detailed chemical equilibrium model for porous ablative materials, Int. J. Heat Mass Tran. 90 (2015) 1034–1045, https://doi.org/10.1016/j.ijheatmasstransfer.2015.05.106.
[36] J. Lachaud, N.N. Mansour, Porous-Material analysis toolbox based on OpenFOAM and applications, J. Thermophys. Heat Tran. 28 (2014) 191–202, https://doi.org/10.2514/1.T4262.
[37] J. Lachaud, J.B. Scoggins, T.E. Magin, M.G. Meyer, N.N. Mansour, A generic local thermal equilibrium model for porous reactive materials submitted to high temperatures, Int. J. Heat Mass Tran. 108 (2017) 1406–1417, https://doi.org/10.1016/j.ijheatmasstransfer.2016.11.067.
[38] J. Huang, W.-X. Yao, X.-Y. Shan, C. Chang, Coupled fluid–structural thermal numerical methods for thermal protection System, AIAA J. 57 (2019) 3630–3638, https://doi.org/10.2514/1.J057616.
[39] Y. Wang, T.K. Risch, C.L. Pasiliao, Modeling of pyrolyzing ablation problem with ABAQUS: a one-dimensional test case, J. Thermophys. Heat Tran. 32 (2018) 544–546, https://doi.org/10.2514/1.T5274.
[40] R.D. Mathieu, Mechanical spallation of charring ablators in hyperthermal environments, AIAA J. 2 (1964) 1621–1627, https://doi.org/10.2514/3.2629.
[41] J.A. Dec, R.D. Braun, B. Laub, Ablative thermal response analysis using the finite element method, J. Thermophys. Heat Tran. 26 (2012) 201–212, https://doi.org/10.2514/1.T3694.
[42] J.M. Lenoir, G. Robillard, A mathematical method to predict the effects of erosive burning in solid-propellant rockets, Symposium (International) on Combustion 6 (1957) 663–667, https://doi.org/10.1016/S0082-0784(57)80092-7.
[43] C.B. Moyer, R.A. Rindal, An analysis of the coupled chemically reacting boundary layer and charring ablator. Part 2- Finite Difference Solution for the In-Depth Response of Charring Materials Considering Surface Chemical and Energy Balances, 1968.
[44] L.A. Dombrovsky, Radiation Heat Transfer in Disperse Systems, first ed., Begell House Inc. Publ., New York, 1995.
[45] F. Ponti, S. Mini, A. Annovazzi, Numerical evaluation of the effects of inclusions on solid rocket motor performance, AIAA J. 58 (2020) 4028–4036, https://doi.org/10.2514/1.J058735.
[46] B.A. Bodhaine, N.B. Wood, E.G. Dutton, J.R. Slusser, On rayleigh optical depth calculations, J. Atmos. Ocean. Technol. 16 (1999) 1854–1861, https://doi.org/10.1175/1520-0426(1999)016<1854:ORODC>2.0.CO;2.
[47] Inc. ANSYS, ANSYS Fluent User's Guide, 17.2, Release, 2016.
[48] Y.-K. Chen, F.S. Milos, Navier-Stokes solutions with finite rate ablation for planetary mission Earth reentries, J. Spacecraft Rockets 42 (2005) 961–970, https://doi.org/10.2514/1.12248.
[49] S.D. Williams, D.M. Curry, Thermal Protection Materials, 1992.
[50] C. Boor, A Practical Guide to Splines, first ed., Springer, New York, 2001.
[51] F.E.C. Culick, A review of calculations for unsteady burning of a solid propellant, AIAA J. 6 (1968) 2241–2255, https://doi.org/10.2514/3.4980.